ACS Catalysis

pubs.acs.org/acscatalysis
Research Article

Bridging Oxide Thermodynamics and Site-Blocking: A Computational Study of ORR Activity on Platinum Nanoparticles

Tom Demeyere, Tom Ellaby, Misbah Sarwar, David Thompsett, and Chris-Kriton Skylaris*

Cite This: ACS Catal. 2025, 15, 5674−5682
Read Online

ACCESS | Metrics & More | Article Recommendations | Supporting Information

ABSTRACT: The oxygen reduction reaction (ORR) is a key reaction in fuel cells and metal−air batteries, where high overpotentials remain a critical challenge despite extensive research. While experimental studies have revealed the importance of surface oxidation, a unified computational framework capable of simultaneously capturing both the thermodynamic aspects of rate-determining steps and the kinetic effects of site-blocking on the overpotential has remained elusive. In this work, we present a computational approach that bridges this gap by combining grand-canonical Monte Carlo simulations with the MACE-MP-0 foundation model to study the ORR on experimentally reconstructed Pt nanoparticles. This framework enables the systematic investigation of oxidation effects across multiple scales, from atomic-level place-exchange mechanisms to macroscopic kinetic behavior. Our simulations reveal a strong dependence of system thermodynamics on oxygen coverage and successfully predict the place-exchange mechanism onset at 1.06 V vs SHE, in agreement with experimental observations. Through established scaling relations and deletion energy analysis, we quantify both the rate-determining step and the distribution of reactive sites on the oxidized surface, providing insight into the complex interplay between surface oxidation and ORR activity. By linking our results with both theoretical and experimental benchmarks on multiple points, we ensure the viability of our assumptions and approach. Using a simplified kinetic model derived from our simulations, we demonstrate agreement with core experimental observations, illustrating how computational approaches based on foundation models can enhance our understanding of catalytic processes. This work not only provides a comprehensive understanding of oxide effects in ORR but also establishes a versatile computational methodology that can be readily extended to study similar electrochemical processes on other catalytic systems, offering a powerful tool for rational catalyst design.

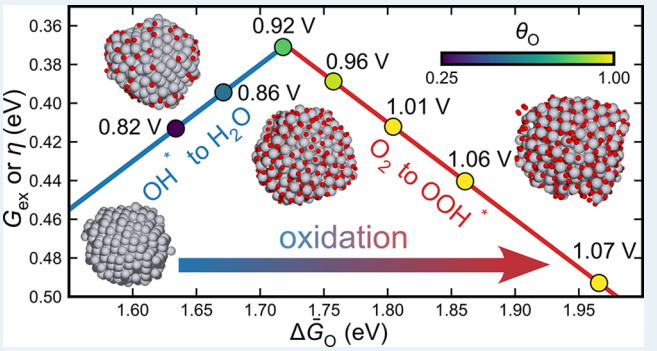

KEYWORDS: *ORR, nanoparticles, oxidation, site-blocking, overpotential, Monte Carlo, MACE-MP-0, DFT*

INTRODUCTION

Understanding the overpotential of the Oxygen Reduction Reaction (ORR) at the cathode of Proton Exchange Membrane Fuel Cells (PEMFC) has been the focus of extensive research efforts.[1−4] The framework introduced by Nørskov et al.[5] which uses thermodynamic arguments to explain the overpotential is particularly insightful and has been used by numerous studies[1,6−11] highlighting its significance in the field. Yet, alternative explanations for the overpotential have been explored to provide a more comprehensive understanding of the ORR. Notably, the presence of site-blocking species[3,12,13] and parasitic reactions leading to mixed potentials.[14] It has been shown that the ORR indeed proceeds more slowly on oxidized platinum catalysts.[15,16] Similarly, it has been shown that specific intermediates can participate in nonelectrochemical reactions[17] such as the hydrolysis of O* further reducing the efficiency of the system. It is increasingly evident that the general solution to the ORR overpotential prediction likely lies in a combination of these factors.

In the field of computational electrochemistry, methodologies are still maturing, and predicting electrochemical properties is difficult.[18] This is the consequence of both cost and numerical complexity linked to the modeling of reactions in an electrochemical setup[19] where the applied potential is a crucial variable. Therefore, computationally elucidating the complex interplay between the various factors governing the ORR is most challenging. In this work, we start by generating oxidized configurations of an experimentally reconstructed Pt_{353} nanoparticle[20] by performing Grand-Canonical minimization Monte Carlo simulations using the recent MACE-MP-0 foundation model. MACE is a message-passing version of the

Received: January 13, 2025
Revised: March 17, 2025
Accepted: March 17, 2025
Published: March 21, 2025

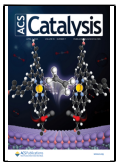

Atomic Cluster Expansion (ACE), and has been recently trained on the material project database at the DFT (PBE+U) level of theory. The resulting foundation model is thus primarily trained on crystal structures, with an emphasis on oxide materials, which motivated its use in this study. For more information about the models and the MACE theory, the reader is redirected toward the original publications and reviews.[21,22]

We use simple arguments to compute thermodynamic and structural properties versus applied potential. Our model correctly predicts the formation of a stable oxide-like phase at high potentials with the presence of a place-exchange mechanism occurring at 1.06 V vs SHE close to the onset potential of the ORR, in good agreement with experimental estimates. Additionally, using previously established scaling relations we find the Rate-Determining Step (RDS) on the oxidized catalyst to be the initial reduction of O_2 to OOH*. Finally, we discuss contrasting views, with the reported possibility of nonoxide oxygenated species on specific catalysts, leading to increased activity.

Attempting to progress toward the unification of various kinetic and thermodynamic aspects of the ORR we fully parametrize a simplified kinetic model which depends on the presence of site-blocking species. The parameters along with their variations with applied potential are directly derived from our simulations. The presented results and methodologies are a step toward the understanding of the various aspects causing the overpotential of the ORR through atomistic modeling.

METHODS

The simulation is performed on an experimentally reconstructed Pt_{353} nanoparticle, which has been shown to display geometric features not observed in perfect shapes.[20] We aim to retrieve plausible oxidized configurations for the nanoparticle by performing a Grand Canonical minimization Monte Carlo simulation using the recent MACE-MP-0 foundation model. The simulation is performed using a temperature of 350 K and an oxygen pressure of 1 atm. The large foundation model is used without dispersion correction, and using the double type precision *float64*. More information and details about these parameters can be found in the Supporting Information.

To compare the energies given by the MACE-MP-0 force field, we perform DFT calculations on the same configurations using the Quantum Espresso v7.3 package.[23,24] The pseudopotentials are taken from the SSSP efficiency library,[25] that is USPP (GBRV 1.4) for Pt,[26] and PAW (pslibrary-0.3.1) for O.[27] The wave function cutoff was chosen as 60 Ry, and the charge density cutoff to be equal to 480 Ry. The unit cell is chosen such that each image has a minimum of 18 Å with its neighbors, no boundary condition correction has been applied. The calculations are carried using the PBE functional. The occupations are smeared using a cold smearing of 0.01 Ry.

The additional geometry optimizations are done using the Quantum Espresso internal BFGS algorithm, the energy criterion is set to 5.0×10^{-3} Ry and the force criterion is set to 0.01 Ry/Bohr. Due to the high cost of these calculations, we only run a limited amount of BFGS steps depending on the system size. This allows us to partially optimize the configurations, while reducing the computational cost by only including the most important geometry steps. We find that the first geometry steps are crucial to relax the Pt skeleton due to lattice mismatch between DFT and MACE-MP-0. Most importantly, we do not observe significant changes in the oxygen positions (sites) throughout the geometry optimizations. Additional details, including the number of geometry steps, maximum forces, last energy changes, and comparison with the single-point energy for each configuration are available in the Supporting Information.

RESULTS

Thermodynamic Analysis. We begin our analysis by examining 31 oxidized configurations selected from the Monte Carlo simulation, spanning a range from 383 to 896 atoms. These configurations form the foundation for our subsequent thermodynamic and electronic analyses. Due to the difficulties associated with calculating coverage for configurations including subsurface and core oxygen atoms, we refer to our systems using the concept of oxygen ratio (N_O/N_{Pt}).[28,29] When needed, the coverage was estimated by using a technique involving the alpha shape to find both oxygen and platinum atoms at the outer shell of the nanoparticles (Supporting Information). For all our oxidized configurations the Gibbs free energy per oxygen atom was calculated using eq 1.

$$\Delta\bar{G}_O \equiv \frac{\Delta G_O}{n} = \frac{1}{n}(E_{nO*} - E_* - nG_{H_2O} + nG_{H_2}) \quad (1)$$

where E_{nO*} is the total energy of the oxidized nanoparticle, E_* is the energy of the clean nanoparticle, and G_{H_2O}, G_{H_2} are the Gibbs free energies of gaseous water and dihydrogen, respectively. For the latter two, zero point energy and entropy contributions are added.[5] eq 1 is obtained by considering a CHE compliant oxidation reaction given by eq 2.

$$Pt^* + nH_2O \rightarrow Pt - O_n + nH_2 \quad (2)$$

The predicted values of $\Delta\bar{G}_O$ using MACE-MP-0 are shown in Figure 1 for the 31 configurations. We find the descriptor

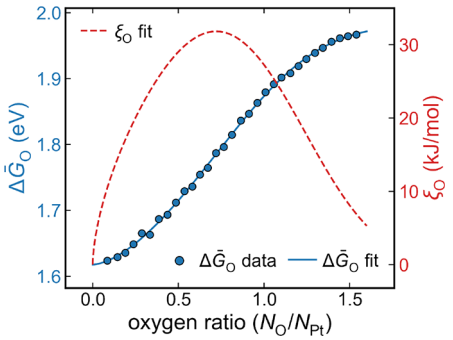

Figure 1. Oxygen Gibbs free energy $\Delta\bar{G}_O$ per atom (blue circles) and lateral coefficient ξ_O (red dashed line). The blue data points were fitted using a generalized error function (solid blue line), while the red curve represents the direct derivative of this fit with respect to the oxygen ratio.

$\Delta\bar{G}_O$ to highly depend on the oxygen ratio, with the slope of the curve directly giving the lateral interaction coefficient ξ_O. This coefficient is expected to be small at low oxygen ratios, and to progressively increase as oxygen content increases due to modification of the electronic structure of the nanoparticle, and direct interactions between oxygen atoms. We report a similar behavior until an oxygen ratio of ≈0.7, after which the quantity steadily decreases, in relation with the plateauing behavior of the Gibbs free energy at higher oxygen ratios. We

https://doi.org/10.1021/acscatal.5c00321
ACS Catal. 2025, 15, 5674−5682

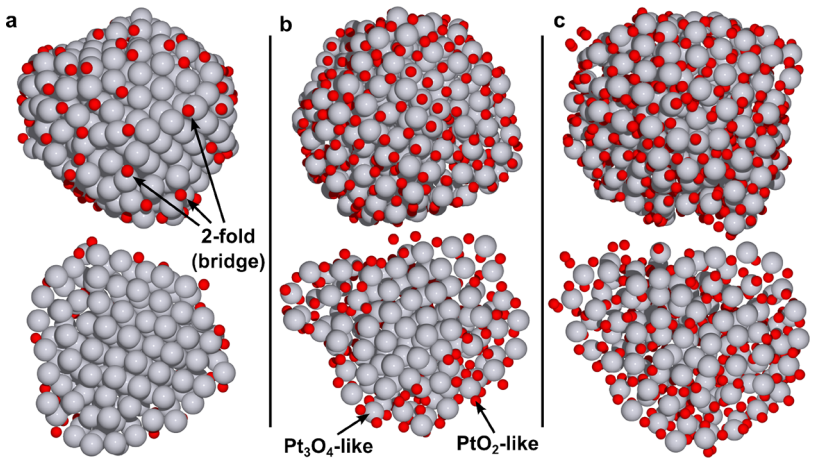

Figure 2. Structural visualization of the Pt_{353} nanoparticle under three distinct oxidation states, characterized by their oxygen ratios (N_O/N_{Pt}) of 0.29 (a), 0.96 (b), and 1.58 (c). The upper panels present complete surface views, while the lower panels display cross-sectional views revealing the internal structure. Platinum atoms are depicted in gray, and oxygen atoms in red.

could not find reports of such decreasing lateral coefficients in the literature, which are typically reported for varying surface coverages of adsorbates on idealized surfaces, significantly differing from the systems investigated in this work. Yet, the range obtained for the lateral coefficient is in good agreement with the expected values for ORR intermediates with values of 0−20 kJ/mol predicted for OH*.[13,30,31] This decrease in lateral coefficient paradoxically suggests that beyond a certain oxygen ratio threshold, the addition of oxygen atoms occurs with diminished resistance. In a recent work, we attributed this phenomenon to the initiation of a stable oxide-like phase at higher oxygen ratios, i.e., as the oxygen content surpasses a critical level, the electronic structure of the Pt skeleton begins to transition, altering the energetics of oxygen incorporation.[32]

Structural Analysis. As illustrated in Figure 2, the structural properties of low oxygen ratio configurations are characterized by surface oxygen atoms on 2-fold, 3-fold or 4-fold coordinated sites. As the oxygen ratio increases, the interaction is increasingly dominated by subsurface oxygen atoms, characterized by square-planar interactions with short bond distances (≤2.0 Å), indicating a Pt_3O_4 stoichiometry. At higher oxygen ratios, a PtO_2 stoichiometry was identified by the formation of PtO_6 octahedrons with two short Pt−O bonds (≈2.0 Å) and four longer bonds (≈2.05 Å).

Locally distinguishing specific phases among the various stoichiometries is challenging and would require detailed analysis using specific descriptors such as the Smooth Overlap of Atomic Positions (SOAP). We attempted to perform classification using such descriptors, but did not reach a valid conclusion, with various configurations showing similarity to multiple phases. This indicates transitional systems with no long-range ordering of the oxide-like phase, and the possibility of multiple phases anchored by dangling oxygen atoms.

Comparison with DFT. Before proceeding to an in-depth analysis, we aim to validate the MACE-MP-0 energies vs DFT (Figure 3). We observe significant discrepancies at low oxygen ratios between the two methods which is not surprising considering that MACE-MP-0 was primarily trained on crystal structures.[33] The agreement with DFT improves as the oxygen ratio increases where configurations are closer to the training set. The parallel behavior observed at higher oxygen ratios indicates that while MACE-MP-0 may not accurately predict absolute energy values, it captures the relative changes in

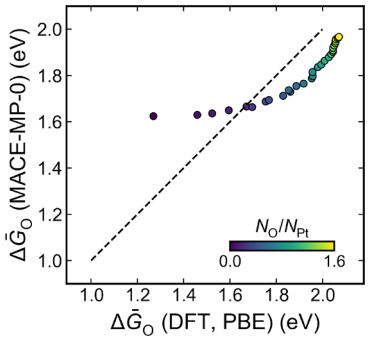

Figure 3. Comparison of oxygen binding descriptor ($\Delta\bar{G}_O$) calculated using DFT versus MACE-MP-0 across various oxidized configurations. Data points are color-coded by oxygen ratio.

energy with increasing oxygen content. The model reliably reproduces energy differences between configurations, which are more pertinent to our study than absolute energy values. This energy difference is most likely due to lattice mismatch between the two methods, leading DFT to predict less stable configurations. We explored this hypothesis by performing additional geometry optimizations using DFT, finding better agreement between the two methods (Supporting Information).

The DFT values obtained in this work at low oxygen ratios ($\Delta\bar{G}_O \approx 1.2$ eV) are −0.3 eV lower than expected values for Pt(111) using the same functional (PBE).[34] In our case this is explained by the large presence of oxygen atoms on 2-fold bridge sites (Figure 2) placed by MACE-MP-0. Such sites have been shown to be more stable than typical 3-fold, fcc or hcp sites by Jennings et al.[35] on a smaller, perfect nanoparticle.[36] Interestingly, MACE-MP-0 did place oxygen atoms on these sites during the Monte Carlo simulations, but could not predict the correct extent of stabilization.

This underscores the challenges associated with accurately computing lateral coefficients for nonideal catalysts, such as our Pt nanoparticle. These difficulties stem from the complex interplay between the varying stabilities of different surface sites and the real interactions among adsorbates. Notably, at low oxygen coverage, a significantly wider range of configurations become accessible, leading to a diverse range of energetically distinct configurations. Consequently, without

https://doi.org/10.1021/acscatal.5c00321
ACS Catal. 2025, 15, 5674−5682

proper sampling, low-oxygen systems can easily exhibit diverse energy landscapes, and our DFT results predict a monotonically decreasing lateral coefficient vs oxygen ratio which can be as high as 250 kJ/mol (Supporting Information). These values are far away from any reasonable estimate produced so far in the literature. Nevertheless, these problems occur at low oxygen ratios ($N_O/N_{Pt} < 0.3$) and are increasingly averaged out as the oxygen ratio increases.

For the purpose of this study we only consider the MACE-MP-0 energies. The force field conveniently gives a smoother picture, removing sites and sampling considerations at low oxygen content. This picture, although less accurate in principle, is more relevant for the study presented here. In any case, this choice does not change our conclusions in any way. The interested reader can find all the DFT results, along with comparable figures in the Supporting Information. A better description most likely lies between the two methods: sites are indeed more stable than predicted by MACE-MP-0, but the lateral coefficient is likely not as high as predicted by DFT due to incorrect sampling, and overestimation of the Pt−O bond stability by the PBE functional.

Oxygen Ratio vs Potential. Using the CHE scheme, we are able to link the potential to the total Gibbs energy ΔG_O (eq 3).

$$\Delta G_O(U_{SHE}) = \Delta G_O - 2nU_{SHE} \tag{3}$$

where U_{SHE} is the desired potential vs SHE, and n is the number of oxygen atoms. By applying this scheme to selected interpolated values of ΔG_O for a grid of U_{SHE}, we obtain a set of linear slopes. From this ensemble, it is possible to predict the most stable oxygen ratio within any given potential range by finding the lowest curve in that interval. Following this approach, the oxygen ratio vs voltage dependence is shown in Figure 4.

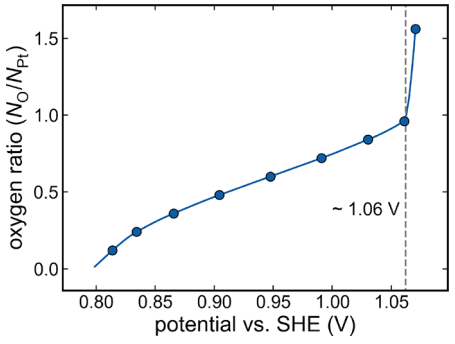

Figure 4. Relationship between electrode potential vs SHE and the oxygen-to-platinum ratio N_O/N_{Pt} showing the potential-dependent evolution of oxygen coverage. The dashed vertical line at ~1.06 V denotes the onset potential for the place-exchange mechanism, marking a transition in the Pt−O interaction.

The onset potential of oxidation is found to be slightly higher than 0.8 V, in reasonable agreement with the existing literature.[4,10,37−39] The oxygen ratio then steadily increases until 1.06 V where it raises sharply. This sudden surge is mathematically explained by the plateauing behavior of the Gibbs energy at high oxygen ratios in Figure 1. This sharp rise, along with the decreasing lateral coefficient indicates the formation of a more stable oxide-like phase. At this point, our thermodynamic model is less relevant, and the system is most likely governed by kinetic effects. These findings align closely with the in situ X-ray absorption spectroscopy experiments conducted by Teliska et al.[40] Their study of platinum particles ranging from 1.5 to 2.5 nm, comparable to our modeled 2.2 nm particle, revealed significant changes in oxygen interactions with platinum around 1.05 V vs RHE. Specifically, the authors observed a shift in the X-ray absorption spectra, indicating a transition from adsorbed oxygen to a more incorporated form, possibly involving oxide formation. Furthermore, their EXAFS data indicated changes in Pt−Pt coordination starting at about 0.90 V, which they attributed to the onset of subsurface oxygen formation. This also corroborates with our computational observations of subsurface oxygen emergence at approximately 0.90 V. This structural reorganization occurring close to 1.05 V is often termed "place-exchange" and has also been reported to occur for Pt(111).[41,42] The reported potential of place-exchange is close to the onset potential of the ORR on platinum-based catalysts, suggesting a connection between the formation of a stable oxide-like phase close to 1.06 V and the overpotential of the ORR on Pt catalysts.

Volcano Plot Analysis. Now that we are able to link oxygen ratio to potential, we can investigate how surface oxidation affects the ORR activity through both site-blocking and thermodynamic effects. To characterize the relative importance of these effects, we first construct a volcano plot by following established methodologies from previous studies,[43,44] assuming that the scaling relations hold for our oxidized catalysts and given by eqs 4a and 4b.

$$\Delta \bar{G}_{OH} = 0.5\Delta \bar{G}_O + K_{OH} \tag{4a}$$

$$\Delta \bar{G}_{OOH} = 0.5\Delta \bar{G}_O + K_{OOH} \tag{4b}$$

Systematic studies conducted on various catalyst types including metal oxides and elemental surfaces have shown the difference between the two constants to be $K_{OOH} - K_{OH} \approx 3.2$ eV.[2,43,44] In contrast, the ideal catalyst, where all elementary steps are isoenergetic should have $K_{OH} = 0$ eV and $K_{OOH} = 2.46$ eV. The main consequence of such scaling relations is the appearance of a minimum inaccessible free energy G_{ex}. This term is the minimum potential difference from equilibrium at which all reactions are downhill in energy and is frequently related to the overpotential η. We expressed G_{ex} as a function of $\Delta \bar{G}_O$ in Figure 5 along with the change in

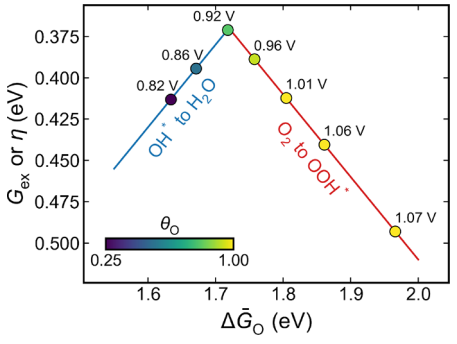

Figure 5. Volcano plot illustrating the relationship between the descriptor $\Delta \bar{G}_O$ and the overpotential η based on OH* and OOH* scaling relations (eqs 4a and 4b). The plot demonstrates how the descriptor $\Delta \bar{G}_O$ evolves with increasing oxygen surface coverage (θ_O, color bar), with corresponding predicted potential values (labeled in volts) obtained using Figure 4. The RDS shift from OH* to H_2O (blue line) to O_2 to OOH* (red line) is clearly observed.

https://doi.org/10.1021/acscatal.5c00321
ACS Catal. 2025, 15, 5674−5682

$\Delta\bar{G}_O$ for selected oxygen coverages. Two regimes can be identified: for catalysts that bind oxygen too strongly, the Rate-Determining Step (RDS) is the conversion of OH* to H_2O, while for catalysts with weak oxygen binding, the formation of OOH* from O_2 becomes rate-limiting.

At low coverages $\Delta\bar{G}_O$ is lower than the optimal value of 1.73 eV, as expected for Pt. However, this quickly changes as the coverage increases; a direct consequence of the $\Delta\bar{G}_O$ variations vs oxygen ratio, expressed as coverage here. As the oxygen coverage, and therefore the potential increases, the descriptor shifts toward the right side of the volcano plot. At higher potentials, the descriptor $\Delta\bar{G}_O$ is too high, and the limiting reaction is expected to be the formation of OOH* from O_2. This is explained by the overall weaker binding on the oxide covered catalyst, which was also reported by previous DFT studies.[10,45] Therefore, in this picture the significant overpotential of the ORR is linked to both site-blocking and thermodynamic considerations, both due to the presence of oxide species. The expected Gibbs free energy $\Delta\bar{G}_O$ on the oxidized catalyst is too high, and the reaction cannot initiate.[46] This is either caused by the inability of O_2 to adsorb, or to be reduced to OOH*. Prior studies reported the same RDS on (oxidized)-platinum catalysts.[13,17,47] Tripkovic and Vegge[9] showed unfavorable binding of O_2 on oxide covered Pt surfaces, along with the activation energy increase for OOH* formation.

In this regime, both forward $k_{\rightarrow O*}$ and inverse $k_{O*\rightarrow}$ rate constant of oxygen formation and dissociation are expected to be impactful. Additionally, as previously stated the reaction cannot initiate, and the rate constant $k_{O_2\rightarrow OOH*}$ plays a critical role. Therefore, the rate of reaction at high potentials is expected to be mainly influenced by the ratio of these constants (eq 5).

$$\nu_{ORR} \propto \frac{k_{O_2\rightarrow OOH*}k_{O*\rightarrow}}{k_{\rightarrow O*}} = k^*_{O_2\rightarrow OOH}K_{O*\rightarrow} \tag{5}$$

This view directly correlates with the work of Huang et al.[13] where the authors found similar relations at high potentials, with the addition of constants involved in the formation of OH*. Therefore, the lack of this species in our simulation can be seen as a limitation. Another limitation is the lack of direct kinetic aspect of our Monte Carlo simulations as experimental studies have shown oxidation to be time dependent.[4,48] Instead, we are limited to the pure thermodynamic picture which is not likely representative of real conditions. As a result, the sharp oxidation peak visible in our framework might be attenuated or smoothed by kinetic effects under specific experimental conditions.

Deletion Energy Analysis. It was noticed by multiple studies that presence of oxygenated species on the catalyst does not always reduce catalytic activity.[47,49,50] Gómez-Marín et al.[50] discussed the importance of distinguishing between the presence of adsorbed oxygenated species and the presence of a stable oxide-like phase. To quantitatively assess the distribution and strength of site blocking effects, we perform a deletion energy analysis across our oxidized configurations. For each of our configurations we manually remove surface oxygen one after the other and calculate the predicted deletion energies ΔG_O^{del} (eq 6).

$$\Delta G_O^{del} = E_{nO*} - E_{(n-1)O*} - G_{H_2O} + G_{H_2} \tag{6}$$

Geometry optimizations were performed for each deletion to reach a local energy minimum. The distribution of deletion energies for selected configurations are presented in Figure 6. The histograms reveal that ΔG_O^{del} spans a vast range of energies for all configurations, with values varying from below 1.0 eV to above 2.0 eV.

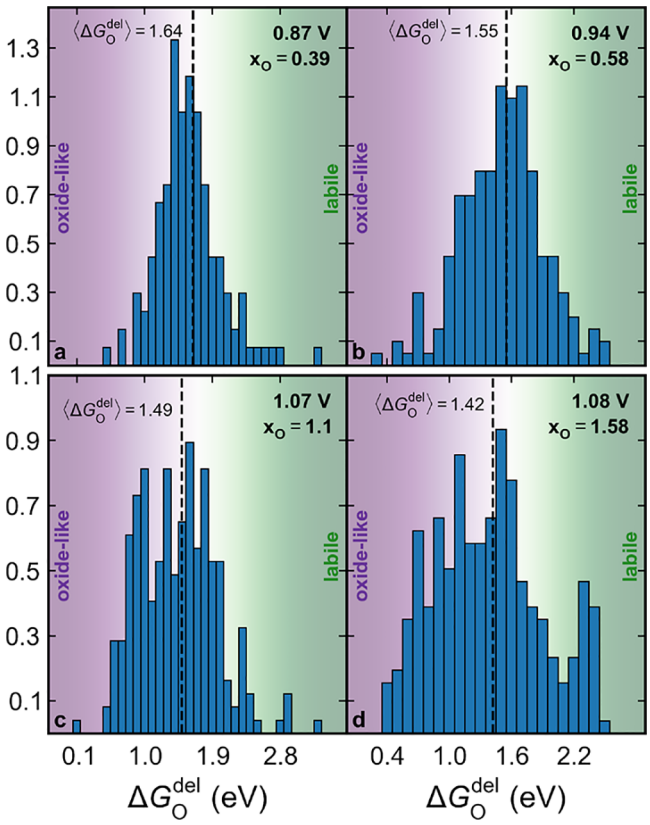

Figure 6. Deletion analysis histogram for four selected configurations at different oxygen ratios $x_O \equiv N_O/N_{Pt}$, (a) 0.39, (b) 0.58, (c) 1.1, and (d) 1.58, with predicted electrochemical potentials indicated for each case. The mean deletion energy is shown by the vertical dashed line. Only outer-shell oxygen atoms were considered in the analysis to avoid biasing the results. The CHE is not applied on the energies to allow for a direct comparison between configurations.

Sites exhibiting lower deletion energies effectively act as reaction inhibitors, blocking the reaction, while higher energy sites suggests availability for further reduction. Figure 6 suggests increasing site blocking as the oxygen ratio increases as supported by the decreasing average deletion energy $\langle\Delta G_O^{del}\rangle$ with increasing oxygen ratio. This decrease corroborates with the gradual formation of a stable oxide-like phase mentioned previously. Conversely, it is harder to add reactants due to the increase of $\Delta\bar{G}_O$ in Figure 1. The two statements can be perceived as contradictory but are consistent with the Monte Carlo approach. As the simulation progresses, it is harder to add oxygen atoms, and the simulation converges to a specific atomic count. Similarly, weaker-bound atoms are deleted first, and the average deletion energy decreases.

This observation indeed suggests that oxygen species do not uniformly act as site-blockers on the nonideal Pt_{353} nanoparticle. Rather, specific sites remain available for reduction, a phenomenon increasingly pronounced as the potential lowers. If we naively follow the CHE framework and consider the main

https://doi.org/10.1021/acscatal.5c00321
ACS Catal. 2025, 15, 5674−5682

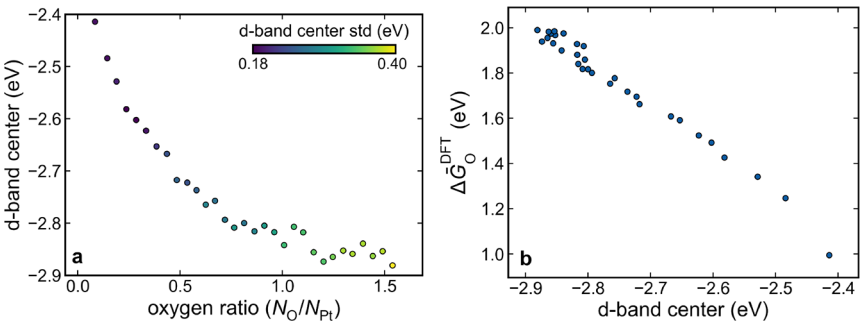

Figure 7. (a) Variation of the d-band center of Pt atoms at the outer shell of the nanoparticle with oxygen ratio. Colors indicate the standard deviation of d-band center in the sample. (b) Correlation between the d-band center and the oxygen binding descriptor calculated with DFT $\Delta\bar{G}_O^{DFT}$.

condition for reduction to be $\Delta G_O^{del} > 2U$ then, at 0.8 V, 56% of species should be able to be reduced versus 35% for 0.87 V, and 9% for 1.07 V. Hence, it might be desirable to design catalysts which lower the presence of stable oxide-like species, without necessarily lowering the overall oxygen coverage.[47] This can be done by finding a catalyst showing resistance to oxidation, therefore changing the slope of $\Delta\bar{G}_O$ in Figure 1.

Electronic Structure Analysis. We now turn our attention to the electronic structure of the oxidized configurations, aiming to further solidify the picture given by our previous analysis. Using the DFT calculations done to benchmark the MACE-MP-0 model, we computed d-band centers for the 31 oxidized configurations, a well-known descriptor used to predict the binding of simple adsorbate.[5,51] Figure 7a shows the average d-band center for platinum atoms lying on the surface of the nanoparticle for each configuration. As the oxygen content increases, the d-band center of the Pt atoms shifts to lower energies, indicating weaker binding. As the oxygen ratio surpasses 0.7, the d-band center begins to stabilize, suggesting that the effect of oxygen incorporation on the electronic structure of the outer shell is less pronounced at higher oxygen ratios. Additionally, the distribution of d-band centers broadens, as suggested by the increasing standard deviation, indicating the presence of multiple oxygenated species with varying binding strengths, in line with the broad distribution of deletion energies observed in Figure 6.

The correlation between $\Delta\bar{G}_O$ and the d-band center of atoms located at the outer shell of the nanoparticle shown in Figure 7b provides two important insights. First, it gives strong evidence for the effects of oxygen content on the thermodynamics of the catalyst at the surface level, which was not entirely clear until now since the descriptor $\Delta\bar{G}_O$ is averaged over all oxygen atoms. Second, it demonstrates that changes in the descriptor are fundamentally linked to the electronic structure of the platinum skeleton, which evolves with oxygen coverage.

This view correlates with the arguments presented in a recent study by Brandes et al.,[52] which demonstrated that on polycrystalline platinum, O species influence ORR primarily through electronic effects. Our calculations provide atomic-scale insight into such observations: the progressive shift in d-band center with increasing oxygen coverage directly impacts binding energies of reaction intermediates, deactivating sites. However, in their study, the authors intentionally avoided higher potentials to prevent formation of stronger oxide species. This suggests that site-blocking is only dominant at very high potentials where oxide-species form, as indicated by our deletion energy analysis. This argumentation contrasts with the view that O species block sites mainly via steric arguments, e.g., conventional "site-blocking", and provides a more nuanced picture of the interplay between oxygen species, electronic structure, and catalyst activity.

Our analysis highlights the difficulties associated with comprehensively characterizing the exact nature of oxygenated species on the catalyst. These challenges arise from the simultaneous presence of many types of oxygenated species, particularly at higher coverages where the Pt skeleton displays a diverse electronic structure. This picture increases in complexity as such a variety of species will interact differently with electrochemical phenomena (here absent) in various ways, leading to a range of observable effects.

By investigating the electronic structure of the catalyst, we again find a transition point marking the boundary between two regimes. The breaking point is related to the place-exchange mechanism, where the d-band centers stabilize but show increased standard deviation. This point marks the formation of an oxide phase, greatly inhibiting the reaction due to the presence of stable oxide species, as also suggested by the deletion energy analysis. At this point, the electronic effect leaves the scalability regime, and the effects on $\Delta\bar{G}_O$ become less clear, as shown in Figure 7b.

In this section, we link the previous thermodynamic analysis to the electronic structure of the catalyst. This analysis explain why different studies might observe varying mechanisms: the dominant effect most likely depends on the specific coverage regime, surface structure, and experimental conditions being probed. Rather than viewing electronic modification and site blocking as competing mechanisms, our results suggest they are complementary effects whose relative importance varies with coverage and potential.

Kinetic Model. Having established the thermodynamic and electronic effects of surface oxidation, we now incorporate these insights into a kinetic model by expressing current density as a function of blocking oxide species. Following established approaches,[37−39] we introduce this contribution as a prefactor term in eq 7, where the current density is expressed as a function of the applied potential.

$$j(U) = j_0(1 - \gamma\theta_O(U))^n \exp\left(\frac{-\xi_O(U)\theta_O(U)}{k_B T}\right) \exp\left(\frac{U - U_{ORR}^{\circ}}{k_B T}\right) \quad (7)$$

https://doi.org/10.1021/acscatal.5c00321
ACS Catal. 2025, 15, 5674−5682

where γ is the site-blocking coefficient, θ_O is the oxygen coverage, n is the number of Pt site involved in the RDS, and U°_{ORR} is the equilibrium potential here taken as 1.23 V. We write the prefactor j_0 to be a function of the total density of site per unit area (eq 8).

$$j_0 = \bar{j}_0 \exp\left(\frac{-\Delta G^{\ddagger}_{ORR}(0)}{k_B T}\right) = 2ek_0 \frac{N_{site}}{A} \exp\left(\frac{-\Delta G^{\ddagger}_{ORR}(0)}{k_B T}\right) \quad (8)$$

where e is the elementary charge, k_0 = 200/s/site is the exchange rate, N_{site} is the total number of sites and A is the surface area (both calculated from the alpha shape technique), giving $\bar{j}_0$ to be 121 mA/cm^2. The value of k_0 was taken from a study of Nørskov et al.[53] where the authors performed a fitting using multiple metals to obtain a plausible value.

Following eq 8, j_0 is calculated using the activation energy of the RDS on the oxide-free catalyst $\Delta G^{\ddagger}_{ORR}(0)$ at the equilibrium potential U°_{ORR}. This value is challenging to obtain experimentally since the catalyst is fully oxidized at this potential. Instead, we estimate this value based on theoretical literature and eq 9.

$$\Delta G^{\ddagger}_{ORR}(\theta_O) = \Delta G^{\ddagger}_{ORR}(0) + \xi_O(\theta_O(U))\theta_O(U) \quad (9)$$

where ξ_O is the lateral coefficient from the first part of this work. Considering that $\Delta G^{\ddagger}_{ORR}(\theta_O = 1)$ is 0.6−0.8 eV[54,55] experimentally, and eq 9 suggests a 0.35 eV increase at full coverage, we selected $\Delta G^{\ddagger}_{ORR}(\theta_O = 0)$ values in the 0.2−0.4 eV range, in line with theoretical values for O_2 protonation.[9,56−58] For example, applying eq 9 to $\Delta G^{\ddagger}_{ORR}(0)$ = 0.30 eV, gives $\Delta G^{\ddagger}_{ORR}(1.0)$ = 0.65 eV, in agreement with the early experimental literature which estimated the oxide-covered barriers to be 0.62,[59] 0.76,[60] or 0.87 eV.[54]

As previously discussed, depending on the potential U, not all oxide species are site-blocking. However, to avoid additional complexities and assumptions, we opted for a simpler approach and used a constant value of γ = 0.66. We take n equal to 2, as two platinum sites are required for the RDS at high potentials.

Finally, in Figure 8 we plot eq 7 for our chosen values of $\Delta G^{\ddagger}_{ORR}(0)$ and obtain plausible current densities versus potential curves. Comparison with the existing experimental literature can be made by using the current density value at 0.9 V $j(0.9)$ which has been reported by various studies to be between 0.1 and 0.4 mA/cm^2 for standard Pt/C catalysts.[61] This suggests, by considering Figure 8 that the activation energy of the RDS on the oxide-free catalyst is indeed between 0.25 and 0.35 eV, giving an estimate of the activation barrier on the oxide covered catalyst between 0.6 and 0.7 eV. Considering both reasonable agreements with the existing literature for $\Delta G^{\ddagger}_{ORR}$ and $j(0.9)$, we argue that our various assumptions made in the kinetic model are justified and lead to a plausible representation of the polarization curve.

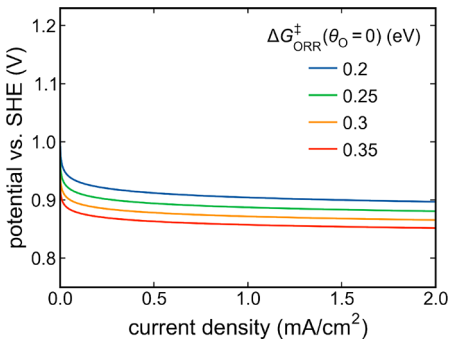

Figure 8. Current density−potential curves predicted by the kinetic model. Different colors represent distinct activation energy values, illustrating the systematic effect of this parameter.

The kinetic model is highly dependent on both the coverage prefactor and the chosen activation energy. Improvements would likely require a more detailed study of the various parameters and their delicate balance. Considering that our Monte Carlo simulation samples the thermodynamic limit, it is likely to overestimate the impact of site-blocking. Therefore, it might be desirable to use alternative computational methods to help balance kinetic and thermodynamic aspects. Nevertheless, our approach gives convincing results and offers a solid foundation for understanding ORR overpotential. To further refine our model, future work could explore a broader range of parameters, improve the assumptions made about the activation energies, and more importantly, perform additional sampling with fine-tuned force fields. Such enhancements would help to understand the precise nature and relative weight of the various factors in eq 7.

CONCLUSIONS

This study presents a novel approach which makes use of simple arguments and assumptions to improve our understanding of the ORR overpotential on Pt-based catalysts through atomistic modeling. Our work unifies the thermodynamic aspects of the overpotential, as described by known scaling relations and the CHE, with kinetic limitations via site-blocking arguments. We show that both are caused by the same phenomenon: the formation of oxide-like species on the catalyst at high potentials. This unified treatment of thermodynamic and kinetic effects through the lens of oxide formation represents a significant departure from traditional approaches that treat these phenomena separately, offering new insights into the fundamental mechanisms of ORR catalysis. On multiple points we link our results with existing phenomena described in the literature, such as the place-exchange mechanism and the RDS on the oxide covered catalyst. Similarly, numerical values provided by our model are close to known values; the onset potential of oxidation is close to 0.8 V, the place-exchange mechanism is found close to 1.05 V, the activation energy of the RDS on the oxide-covered catalyst is between 0.6 and 0.7 eV, and the current density at 0.9 V is between 0.1 and 0.4 mA/cm^2. These values were obtained through simulations using the recent MACE-MP-0 foundation model, providing new quantitative insights that complement existing experimental and theoretical studies in the literature. Using this approach, we effectively explain the significant overpotential of the ORR on Pt-based catalyst by bridging the gap between thermodynamic and kinetic arguments using state-of-the-art ML force field and established theoretical principles.

As demonstrated by Nørskov et al.,[5] catalysts that bind oxygen slightly more weakly than Pt can enhance catalytic activity. Such catalysts would reduce the site-blocking oxygen coverage $\theta_O(U)$ at given potentials and potentially lower the activation energy through more favorable reaction thermodynamics. However, our work suggests that designing oxidation-resistant catalysts may be a more effective strategy. This approach could shift the sharp oxidation transition occurring at

https://doi.org/10.1021/acscatal.5c00321
ACS Catal. 2025, 15, 5674−5682

1.05 V in this work, close to the onset potential of the ORR, toward higher potentials while maintaining a reactive oxygen coverage, thereby reducing the site-blocking coefficient at high potentials and ultimately enhancing catalytic activity.

With the recent advances in the field of material science and modeling, it becomes increasingly feasible to perform computationally complex workflows leading to detailed and fully parametrized kinetic models. The model presented in this study can be improved on multiple points, for example by including OH* species in the simulations, or by using more complex computational methods aiming for a better sampling or to introduce kinetic aspects. More importantly, future work should focus on fine-tuning the foundation model to better describe the energetics of these systems. By providing insights into the capabilities and limitations of such computational workflows, our study aims to pave the way for targeted computational investigations of other complex electrocatalytic processes, particularly those involving dynamic surface restructuring and competing reaction pathways at different potential ranges.

■ ASSOCIATED CONTENT

Data Availability Statement

The data underlying this study are openly available at the following DOI: 10.5281/zenodo.14621239.

Supporting Information

The Supporting Information is available free of charge at https://pubs.acs.org/doi/10.1021/acscatal.5c00321.

Details on coverage estimation methods, Monte Carlo simulation procedures, DFT comparisons, and DFT-calculated versions of all main text figures (PDF)

■ AUTHOR INFORMATION

Corresponding Author

Chris-Kriton Skylaris − *School of Chemistry, University of Southampton, Southampton SO17 1BJ, United Kingdom;* orcid.org/0000-0003-0258-3433; Email: C.Skylaris@soton.ac.uk

Authors

Tom Demeyere − *School of Chemistry, University of Southampton, Southampton SO17 1BJ, United Kingdom;* orcid.org/0000-0002-5023-6156

Tom Ellaby − *Johnson Matthey Technology Centre, Reading RG4 9NH, United Kingdom*

Misbah Sarwar − *Johnson Matthey Technology Centre, Reading RG4 9NH, United Kingdom*

David Thompsett − *Johnson Matthey Technology Centre, Reading RG4 9NH, United Kingdom*

Complete contact information is available at: https://pubs.acs.org/10.1021/acscatal.5c00321

Notes

The authors declare no competing financial interest.

■ ACKNOWLEDGMENTS

We thank D. Sarpa for useful discussions and E. Gerouville for proofreading. We are grateful for access to the ARCHER2 national supercomputer, which was obtained via the United Kingdom Car-Parrinello Consortium (UKCP) funded by EPSRC (Grant No. EP/X035956/1). We are grateful to the UK Materials and Molecular Modelling Hub for computational resources, which is partially funded by EPSRC(EP/T022213/1, EP/W032260/1, and EP/P020194/1).

■ REFERENCES

(1) Keith, J. A.; Jerkiewicz, G.; Jacob, T. Theoretical Investigations of the Oxygen Reduction Reaction on Pt(111). *ChemPhysChem* **2010**, *11*, 2779−2794.

(2) Kulkarni, A.; Siahrostami, S.; Patel, A.; Nørskov, J. K. Understanding Catalytic Activity Trends in the Oxygen Reduction Reaction. *Chem. Rev.* **2018**, *118*, 2302−2312.

(3) Chen, W.; Huang, J.; Wei, J.; Zhou, D.; Cai, J.; He, Z.-D.; Chen, Y.-X. Origins of High Onset Overpotential of Oxygen Reduction Reaction at Pt-based Electrocatalysts: A Mini Review. *Electrochem. Commun.* **2018**, *96*, 71−76.

(4) Mitzel, J.; Zhang, Q.; Gazdzicki, P.; Friedrich, K. A. Review on Mechanisms and Recovery Procedures for Reversible Performance Losses in Polymer Electrolyte Membrane Fuel Cells. *J. Power Sources* **2021**, *488*, No. 229375.

(5) Nørskov, J. K.; Rossmeisl, J.; Logadottir, A.; Lindqvist, L.; Kitchin, J. R.; Bligaard, T.; Jónsson, H. Origin of the Overpotential for Oxygen Reduction at a Fuel-Cell Cathode. *J. Phys. Chem. B* **2004**, *108*, 17886−17892.

(6) Yeh, K.-Y.; Wasileski, S. A.; Janik, M. J. Electronic Structure Models of Oxygen Adsorption at the Solvated, Electrified Pt(111) Interface. *Phys. Chem. Chem. Phys.* **2009**, *11*, 10108.

(7) Tripković, V.; Skúlason, E.; Siahrostami, S.; Nørskov, J. K.; Rossmeisl, J. The Oxygen Reduction Reaction Mechanism on Pt(111) from Density Functional Theory Calculations. *Electrochim. Acta* **2010**, *55*, 7975−7981.

(8) Lim, D.-H.; Wilcox, J. Mechanisms of the Oxygen Reduction Reaction on Defective Graphene-Supported Pt Nanoparticles from First-Principles. *J. Phys. Chem. C* **2012**, *116*, 3653−3660.

(9) Tripkovic, V.; Vegge, T. Potential- and Rate-Determining Step for Oxygen Reduction on Pt(111). *J. Phys. Chem. C* **2017**, *121*, 26785−26793.

(10) Jinnouchi, R.; Suzuki, K. K. T.; Morimoto, Y. DFT Calculations on Electro-Oxidations and Dissolutions of Pt and Pt−Au Nanoparticles. *Catal. Today* **2016**, *262*, 100−109.

(11) Tripkovic, V. Thermodynamic Assessment of the Oxygen Reduction Activity in Aqueous Solutions. *Phys. Chem. Chem. Phys.* **2017**, *19*, 29381−29388.

(12) Liu, Y.; Mathias, M.; Zhang, J. Measurement of Platinum Oxide Coverage in a Proton Exchange Membrane Fuel Cell. *Electrochem. Solid-State Lett.* **2010**, *13*, B1.

(13) Huang, J.; Zhang, J.; Eikerling, M. Unifying Theoretical Framework for Deciphering the Oxygen Reduction Reaction on Platinum. *Phys. Chem. Chem. Phys.* **2018**, *20*, 11776−11786.

(14) Li, Y.; Liu, Z.-F. Solvated Proton and the Origin of the High Onset Overpotential in the Oxygen Reduction Reaction on Pt(111). *Phys. Chem. Chem. Phys.* **2020**, *22*, 22226−22235.

(15) Wang, Y.; Sun, D.; Wang, M.; Feng, Z.; Hall, A. S. Oxygen Reduction Electrocatalysis on Ordered Intermetallic Pd−Bi Electrodes Is Enhanced by a Low Coverage of Spectator Species. *J. Phys. Chem. C* **2020**, *124*, 5220−5224.

(16) Wu, Z.; Yang, G.; Zhang, Q.; Liu, Z.; Peng, F. Deciphering the High Overpotential of the Oxygen Reduction Reaction via Comprehensively Elucidating the Open Circuit Potential. *Energy Environ. Sci.* **2024**, *17*, 3338−3346.

(17) Tian, F.; Anderson, A. B. Effective Reversible Potential, Energy Loss, and Overpotential on Platinum Fuel Cell Cathodes. *J. Phys. Chem. C* **2011**, *115*, 4076−4088.

(18) Hörmann, N. G.; Andreussi, O.; Marzari, N. Grand Canonical Simulations of Electrochemical Interfaces in Implicit Solvation Models. *J. Chem. Phys.* **2019**, *150*, No. 041730.

(19) Melander, M. M.; Laurila, T. T.; Laasonen, K., Eds. *Atomic-Scale Modelling of Electrochemical Systems*, 1st ed.; Wiley: 2021.

(20) Aarons, J.; Jones, L.; Varambhia, A.; MacArthur, K. E.; Ozkaya, D.; Sarwar, M.; Skylaris, C.-K.; Nellist, P. D. Predicting the Oxygen-Binding Properties of Platinum Nanoparticle Ensembles by

Combining High-Precision Electron Microscopy and Density Functional Theory. *Nano Lett.* **2017**, *17*, 4003−4012.
(21) Batatia, I.; Kovács, D. P.; Simm, G. N. C.; Ortner, C.; Csányi, G. *MACE: Higher Order Equivariant Message Passing Neural Networks for Fast and Accurate Force Fields*. 2023.
(22) Batatia, I.; Batzner, S.; Kovács, D. P.; Musaelian, A.; Simm, G. N. C.; Drautz, R.; Ortner, C.; Kozinsky, B.; Csányi, G. The Design Space of E(3)-Equivariant Atom-Centred Interatomic Potentials. *Nature Machine Intelligence* **2025**, *7*, 56−67.
(23) Giannozzi, P.; et al. QUANTUM ESPRESSO: A Modular and Open-Source Software Project for Quantum Simulations of Materials. *Journal of Physics. Condensed Matter: An Institute of Physics Journal* **2009**, *21*, No. 395502.
(24) Giannozzi, P.; et al. Advanced Capabilities for Materials Modelling with Quantum ESPRESSO. *J. Phys.: Condens. Matter* **2017**, *29*, 465901.
(25) Prandini, G.; Marrazzo, A.; Castelli, I. E.; Mounet, N.; Marzari, N. Precision and Efficiency in Solid-State Pseudopotential Calculations. *npj Comput. Mater.* **2018**, *4*, 1−13.
(26) Garrity, K. F.; Bennett, J. W.; Rabe, K. M.; Vanderbilt, D. Pseudopotentials for High-Throughput DFT Calculations. *Comput. Mater. Sci.* **2014**, *81*, 446−452.
(27) Dal Corso, A. Pseudopotentials Periodic Table: From H to Pu. *Comput. Mater. Sci.* **2014**, *95*, 337−350.
(28) Kirchhoff, B.; Braunwarth, L.; Jung, C.; Jónsson, H.; Fantauzzi, D.; Jacob, T. Simulations of the Oxidation and Degradation of Platinum Electrocatalysts. *Small* **2020**, *16*, No. 1905159.
(29) Kirchhoff, B.; Jung, C.; Jónsson, H.; Fantauzzi, D.; Jacob, T. Simulations of the Electrochemical Oxidation of Pt Nanoparticles of Various Shapes. *J. Phys. Chem. C* **2022**, *126*, 6773−6781.
(30) Climent, V.; Gómez, R.; Orts, J. M.; Feliu, J. M. Thermodynamic Analysis of the Temperature Dependence of OH Adsorption on Pt(111) and Pt(100) Electrodes in Acidic Media in the Absence of Specific Anion Adsorption. *J. Phys. Chem. B* **2006**, *110*, 11344−11351.
(31) Garcia-Araez, N.; Climent, V.; Feliu, J. Potential-Dependent Water Orientation on Pt(111), Pt(100), and Pt(110), As Inferred from Laser-Pulsed Experiments. Electrostatic and Chemical Effects. *J. Phys. Chem. C* **2009**, *113*, 9290−9304.
(32) Demeyere, T.; Islam, H.-U.; Ellaby, T.; Sarwar, M.; Thompsett, D.; Skylaris, C.-K. *Multi-Scale Modeling and Experimental Investigation of Oxidation Behavior in Platinum Nanoparticles*. 2024.
(33) Batatia, I.et al.*A Foundation Model for Atomistic Materials Chemistry*. 2023.
(34) Jinnouchi, R.; Kodama, K.; Morimoto, Y. DFT Calculations on H, OH and O Adsorbate Formations on Pt(111) and Pt(332) Electrodes. *J. Electroanal. Chem.* **2014**, *716*, 31−44.
(35) Jennings, P. C.; Aleksandrov, H. A.; Neyman, K. M.; Johnston, R. L. DFT Studies of Oxygen Dissociation on the 116-Atom Platinum Truncated Octahedron Particle. *Phys. Chem. Chem. Phys.* **2014**, *16*, 26539−26545.
(36) Yohannes, A. G.; Fink, K.; Kondov, I. Pt Nanoparticles under Oxidizing Conditions−Implications of Particle Size, Adsorption Sites and Oxygen Coverage on Stability. *Nanoscale. Advances* **2022**, *4*, 4554−4569.
(37) Markovic, N. Surface Science Studies of Model Fuel Cell Electrocatalysts. *Surf. Sci. Rep.* **2002**, *45*, 117−229.
(38) Xu, Y.; Shao, M.; Mavrikakis, M.; Adzic, R. R. In *Fuel Cell Catalysis*, 1st ed.; Koper, M. T. M., Ed.; Wiley: 2009; pp 271−315.
(39) Gottesfeld, S. *Fuel Cell Catalysis*; John Wiley & Sons, Ltd: 2009; Chapter 1, pp 1−30.
(40) Teliska, M.; O'Grady, W. E.; Ramaker, D. E. Determination of O and OH Adsorption Sites and Coverage in Situ on Pt Electrodes from Pt L_{23} X-ray Absorption Spectroscopy. *J. Phys. Chem. B* **2005**, *109*, 8076−8084.
(41) You, H.; Zurawski, D. J.; Nagy, Z.; Yonco, R. M. *In-Situ* x-Ray Reflectivity Study of Incipient Oxidation of Pt(111) Surface in Electrolyte Solutions. *J. Chem. Phys.* **1994**, *100*, 4699−4702.
(42) You, H.; Nagy, Z. Oxidation-Reduction-Induced Roughening of Platinum (1 1 1) Surface. *Physica B: Condensed Matter* **1994**, *198*, 187−194.
(43) Man, I. C.; Su, H.-Y.; Calle-Vallejo, F.; Hansen, H. A.; Martínez, J. I.; Inoglu, N. G.; Kitchin, J.; Jaramillo, T. F.; Nørskov, J. K.; Rossmeisl, J. Universality in Oxygen Evolution Electrocatalysis on Oxide Surfaces. *ChemCatChem* **2011**, *3*, 1159−1165.
(44) Viswanathan, V.; Hansen, H. A.; Rossmeisl, J.; Nørskov, J. K. Universality in Oxygen Reduction Electrocatalysis on Metal Surfaces. *ACS Catal.* **2012**, *2*, 1654−1660.
(45) Verga, L. G.; Aarons, J.; Sarwar, M.; Thompsett, D.; Russell, A. E.; Skylaris, C.-K. DFT Calculation of Oxygen Adsorption on Platinum Nanoparticles: Coverage and Size Effects. *Faraday Discuss.* **2018**, *208*, 497−522.
(46) Rossmeisl, J.; Logadottir, A.; Nørskov, J. Electrolysis of Water on (Oxidized) Metal Surfaces. *Chem. Phys.* **2005**, *319*, 178−184.
(47) Wakisaka, M.; Suzuki, H.; Mitsui, S.; Uchida, H.; Watanabe, M. Increased Oxygen Coverage at Pt-Fe Alloy Cathode for the Enhanced Oxygen Reduction Reaction Studied by EC-XPS. *J. Phys. Chem. C* **2008**, *112*, 2750−2755.
(48) Conway, B. E.; Barnett, B.; Angerstein-Kozlowska, H.; Tilak, B. V. A Surface-Electrochemical Basis for the Direct Logarithmic Growth Law for Initial Stages of Extension of Anodic Oxide Films Formed at Noble Metals. *J. Chem. Phys.* **1990**, *93*, 8361−8373.
(49) Watanabe, M.; Tryk, D. A.; Wakisaka, M.; Yano, H.; Uchida, H. Overview of Recent Developments in Oxygen Reduction Electrocatalysis. *Electrochim. Acta* **2012**, *84*, 187−201.
(50) Gómez-Marín, A. M.; Rizo, R.; Feliu, J. M. Oxygen Reduction Reaction at Pt Single Crystals: A Critical Overview. *Catalysis Science & Technology* **2014**, *4*, 1685.
(51) Hammer, B.; Nørskov, J. K. *Adv. Catal.*; Impact of Surface Science on Catalysis; Academic Press: 2000; Vol. *45*; pp 71−129.
(52) Brandes, B. A.; Krishnan, Y.; Buchauer, F. L.; Hansen, H. A.; Hjelm, J. Unifying the ORR and OER with Surface Oxygen and Extracting Their Intrinsic Activities on Platinum. *Nat. Commun.* **2024**, *15*, 7336.
(53) Nørskov, J. K.; Bligaard, T.; Logadottir, A.; Kitchin, J. R.; Chen, J. G.; Pandelov, S.; Stimming, U. Trends in the Exchange Current for Hydrogen Evolution. *J. Electrochem. Soc.* **2005**, *152*, J23.
(54) Anderson, A. B.; Albu, T. V. Catalytic Effect of Platinum on Oxygen Reduction An Ab Initio Model Including Electrode Potential Dependence. *J. Electrochem. Soc.* **2000**, *147*, 4229.
(55) Anderson, A. B.; Roques, J.; Mukerjee, S.; Murthi, V. S.; Markovic, N. M.; Stamenkovic, V. Activation Energies for Oxygen Reduction on Platinum Alloys: Theory and Experiment. *J. Phys. Chem. B* **2005**, *109*, 1198−1203.
(56) Duan, Z.; Wang, G. A First Principles Study of Oxygen Reduction Reaction on a Pt(111) Surface Modified by a Subsurface Transition Metal M (M = Ni, Co, or Fe). *Phys. Chem. Chem. Phys.* **2011**, *13*, 20178.
(57) Duan, Z.; Wang, G. Comparison of Reaction Energetics for Oxygen Reduction Reactions on Pt(100), Pt(111), Pt/Ni(100), and Pt/Ni(111) Surfaces: A First-Principles Study. *J. Phys. Chem. C* **2013**, *117*, 6284−6292.
(58) Xiao, B. B.; Jiang, X. B.; Jiang, Q. Density Functional Theory Study of Oxygen Reduction Reaction on Pt/Pd_3 Al(111) Alloy Electrocatalyst. *Phys. Chem. Chem. Phys.* **2016**, *18*, 14234−14243.
(59) Sepa, D.; Vracar, L.; Vojnovic, M.; Damjanovic, A. Symmetry Factor and Transfer Coefficient in Analysis of Enthalpies of Activation and Mechanisms of Oxygen Reduction at Platinum Electrodes. *Electrochim. Acta* **1986**, *31*, 1401−1402.
(60) Parthasarathy, A.; Srinivasan, S.; Appleby, A. J.; Martin, C. R. Temperature Dependence of the Electrode Kinetics of Oxygen Reduction at the Platinum/Nafion® Interface—A Microelectrode Investigation. *J. Electrochem. Soc.* **1992**, *139*, 2530−2537.
(61) Neyerlin, K. C.; Gu, W.; Jorne, J.; Gasteiger, H. A. Determination of Catalyst Unique Parameters for the Oxygen Reduction Reaction in a PEMFC. *J. Electrochem. Soc.* **2006**, *153*, A1955.

https://doi.org/10.1021/acscatal.5c00321
ACS Catal. 2025, 15, 5674−5682